

INTERFACIAL INTERACTIONS OF  
FECO/PD AND FECO/RU  
MULTILAYERS

by

MICHAEL JAMES WALOCK

A THESIS

Submitted in partial fulfillment of the requirements  
for the degree of Master of Science in  
the Department of Physics and Astronomy  
in the Graduate School of  
The University of Alabama

TUSCALOOSA, ALABAMA

2009

Copyright Michael James Walock 2009  
ALL RIGHTS RESERVED

Submitted by Michael James Walock in partial fulfillment of the requirements for the degree of the Master of Science, specializing in Physics.

Accepted on behalf of the Faculty of the Graduate School by the thesis committee:

---

Arunuva Gupta, Ph.D.

---

William H. Butler, Ph.D.

---

Patrick LeClair, Ph.D.

---

Gary J. Mankey, Ph.D.  
Chairperson

---

Raymond White, Ph.D.  
Department Chairperson

---

Date

---

David A. Francko, Ph.D.  
Dean of the Graduate School

---

Date

## LIST OF ABBREVIATIONS AND SYMBOLS

bcc	Body-centered cubic
$\mu_B$	Bohr magneton
AL	Atomic layer
RASCAL	Research and analysis of sputtering conditions at Alabama
XRR	X-ray reflectivity
$\lambda$	Wavelength
$2\theta$	Scattering angle
MOKE	Magneto-optical Kerr effect
VSM	Vibrating sample magnetometry
$M_s$	Saturation magnetization
$H_s$	Saturation field
$H_c$	Coercive field
XMCD	X-ray magnetic circular dichroism
TGM	Toroidal grating monochromator
XAS	X-ray absorption spectra
$\sigma^+$	XAS signal, sample magnetization is parallel to the photon spin
$\sigma^-$	XAS signal, sample magnetization is anti-parallel to the photon spin
$\langle L_z \rangle$	Orbital magnetic moment, in units of $\mu_B$
$\langle S_z \rangle$	Spin magnetic moment, in units of $\mu_B$

$\langle T_z \rangle$	Magnetic dipole term, in units of $\mu_B$
$T_c$	Curie temperature
$m$	Magnetic moment, in units of $\mu_B$
$V$	Volume
$M_r$	Remanent magnetization
PNR	Polarized neutron reflectivity
$R$	Reflectivity
$R_{++}$	Non-spin flip reflectivity: spin up
$R_{--}$	Non-spin flip reflectivity: spin down
$R_{+-}$	Spin flip reflectivity: initial spin up, reflected spin down
$R_{-+}$	Spin flip reflectivity: initial spin down, reflected spin up
$Q$	Momentum transfer, z-component
$Q_c$	Critical edge
$b_n$	Neutron nuclear scattering length
$b_m$	Neutron magnetic scattering length
$\delta_m$	Magnetic scattering length density
$\rho$	Mass density
$M_m$	Molar mass
$N$	Number density
$N_A$	Avogadro's number

## ACKNOWLEDGMENTS

Over the course of my studies at The University of Alabama, I have had the pleasure of knowing many fine individuals amongst the faculty, staff, and my fellow graduate students. For this project, there are many individuals who were invaluable to this research. In particular, I would like to thank the following for their contributions: my thesis committee (Dr. Gary Mankey, Dr. Patrick LeClair, Dr. William Butler, and Dr. Arun Gupta), the instrumentation support staff at the UW-SRC (Mr. Mark Bissen and Ms. Mary Severson), the magnetism reflectometer instrument staff at the SNS (Dr. Haile Ambaye, Dr. Valeria Lauter, and Mr. Rick Goyette), the Physics Machine Shop (David Key, Mike Perrigin and Joe Howell), the Physics Electronics shops (Danny Whitcomb and Jason Kuykendall), the MINT facilities staff (John Hawkins and Jason Foster) and the MINT office staff (Tabatha Jarnagin, Jamie Foster, and Casey McDow). Finally, I would like to thank Jennifer, my wife, for her drive, motivation, and infinite patience.

This research was funded by the NSF Materials Research Science and Engineering Center program through grant NSF-DMR 0213985. Part of this research was performed at the Synchrotron Radiation Center (University of Wisconsin-Madison), operating under NSF grant NSF-DMR 0537588, and at the Spallation Neutron Source (Oak Ridge National Laboratory), supported by the Scientific User Facilities Division, Office of Basic Energy Sciences of the Department of Energy.

## CONTENTS

LIST OF ABBREVIATIONS AND SYMBOLS.....	iii
ACKNOWLEDGMENTS.....	v
LIST OF TABLES.....	vii
LIST OF FIGURES.....	viii
ABSTRACT.....	x
CHAPTER 1: INTRODUCTION.....	1
CHAPTER 2: EXPERIMENTS.....	4
CHAPTER 3: RESULTS AND DISCUSSION.....	20
A. STRUCTURAL CHARACTERIZATION.....	20
B. MAGNETIC CHARACTERIZATION: MOKE.....	22
C. MAGNETIC CHARACTERIZATION: VSM.....	26
D. X-RAY MAGNETIC CIRCULAR DICHROISM.....	30
E. POLARIZED NEUTRON REFLECTIVITY.....	37
CHAPTER 4: CONCLUSIONS.....	43
BIBLIOGRAPHY.....	45

## LIST OF TABLES

<b>Table 1.</b> Summary of MOKE results.....	24
<b>Table 2.</b> Summary of the VSM results for the XMCD samples. Please note, $M_0$ is the saturation magnetization of the FeCo baseline sample.....	27
<b>Table 3.</b> Summary of XMCD results for the calculated magnetic moments. All measurements are in units of $\mu_B$ .....	32

## LIST OF FIGURES

<b>Figure 1.</b> The Slater-Pauling Curve describes the systematic variation in the atomic magnetic moments (in units of $\mu_B$ ), with respect to the number of electrons in the system (Podolak, et al. 2006).....	2
<b>Figure 2.</b> Typical geometry of an x-ray reflectivity (XRR) experiment.....	6
<b>Figure 3.</b> XRR curve of a single layer of $Fe_{65}Co_{35}$ . The Bragg peak analysis technique leads to a film thickness of 24.5 nm. However, this does not provide any quantitative information on the chemical roughness of the sample.....	7
<b>Figure 4.</b> Typical setup of a magneto-optical Kerr effect (MOKE) spectrometer.....	9
<b>Figure 5.</b> Typical set-up for a x-ray magnetic circular dichroism (XMCD) setup in total electron yield (TEY) mode.....	13
<b>Figure 6.</b> X-ray Magnetic Circular Dichroism (XMCD) spectra for the Co calibration sample. (a) shows the normalized x-ray absorption spectra for the two polarization states; (b) is the normalized sum of the two states; and (c) is the normalized difference spectra of the two spectra. The required integrals for the analysis are also shown.....	15
<b>Figure 7.</b> Polarized neutron reflectivity experiments result in four possible cross-sections (Ehlers and Klose 2006). The non-spin flip reflectivities yield information on the magnetic depth profile. The spin-flip cross-sections have information on the surface magnetism.....	19

**Figure 8.** XRR spectra for the Fe<sub>65</sub>Co<sub>35</sub> baseline sample and the two superlattices used in the neutron experiment. The superlattices show Bragg peaks at 4.11 degrees for the FeCo/Pd and at 3.18 degrees for the FeCo/Ru.....21

**Figure 9.** MOKE spectroscopy results on the Fe<sub>65</sub>Co<sub>35</sub> baseline sample and the two superlattices.....25

**Figure 10.** Vibrating sample magnetometry of the XMCD samples The saturation magnetization is normalized to the saturation magnetization of the FeCo baseline sample.....28

**Figure 11.** X-ray Magnetic Circular Dichroism (XMCD) spectra for the FeCo baseline sample. With respect to the Fe edges, (a) shows the normalized x-ray absorption spectra for the two polarization states; (b) is the normalized sum of the two states; and (c) is the normalized difference spectra of the two spectra. The same are shown for the Co edges in (d) to (f). The required integrals for the analysis are also shown.....31

**Figure 12.** Comparison of the difference spectra for (a) the Fe edges and (b) the Co edges in the three samples.....33

**Figure 13.** The non-spin flip reflectivities for the FeCo/Pd at (a) T = 5 K, at (b) T = 300 K, the FeCo/Ru (c) at T = 5 K, and (d) at T = 300 K.....38

**Figure 14.** The reflectivities near the critical edge for the (a) FeCo/Pd and (b) the FeCo/Ru. The red indicates room temperature; the blue indicates low temperature.....42

## ABSTRACT

The FeCo system of alloys is perched atop the Slater-Pauling curve. As a result of this and its relatively low cost and ease of deposition, it is heavily used within the magnetic recording industry. However, new technology requires an advance past this system with respect to high moment, high magnetization materials. One possible step is the enhancement of the FeCo system. One approach is the lamination of thin, nonmagnetic Pd spacer layers with FeCo. Prior published results have shown an increase in not only the moment, but also the magnetization of the samples. We have developed a FeCo/Pd superlattice samples to test this hypothesis. Our results, using a combination of conventional magnetometry, x-ray magnetic circular dichroism, and polarized neutron reflectivity, show a different result from prior reports. The magnetic dichroism experiments show a definite decrease in the magnetic moments of both the Fe and Co with the introduction of Pd. The preliminary analysis of the neutron reflectivity data shows no increase in the magnetic moment of the alloy, nor an induced moment in the Pd. For comparison with the FeCo/Pd superlattice, we studied an antiferromagnetically coupled FeCo/Ru superlattice.

## CHAPTER 1: INTRODUCTION

In the late 1930s, J.C. Slater (Slater 1936) and L. Pauling (Pauling 1938) noticed an interesting phenomenon in the 3d transition metals. There was systematic variation in the atomic magnetic moments with respect to the number of electrons in the atom. The resultant plot is known as the Slater-Pauling curve, Figure 1. As the number of electrons is increased, there is a corresponding increase in the average atomic magnetic moment, until a peak is reached within the FeCo alloy. Past this peak, any increase in the number of electrons results in a decrease in the average atomic magnetic moment of the system.

The bcc-FeCo system is located at the peak of the curve. This, coupled with the relative ease and low-cost of deposition, results in a heavy use by the magnetic recording industry. However, recent technological advances have stretched the system to its magnetic limit. Newer material sets with higher moments, and magnetizations, are required for the next generation of magnetic devices. One possible solution is not a new material set, but an improvement to the current one. Increasing the saturation magnetization of the FeCo alloy system is a possible answer. One approach is the lamination of thin Pd layers with FeCo thin films. The resulting increase in magnetic moment is a magnetic proximity effect. The ferromagnetic FeCo layer induces ferromagnetism in the nonmagnetic Pd layer.

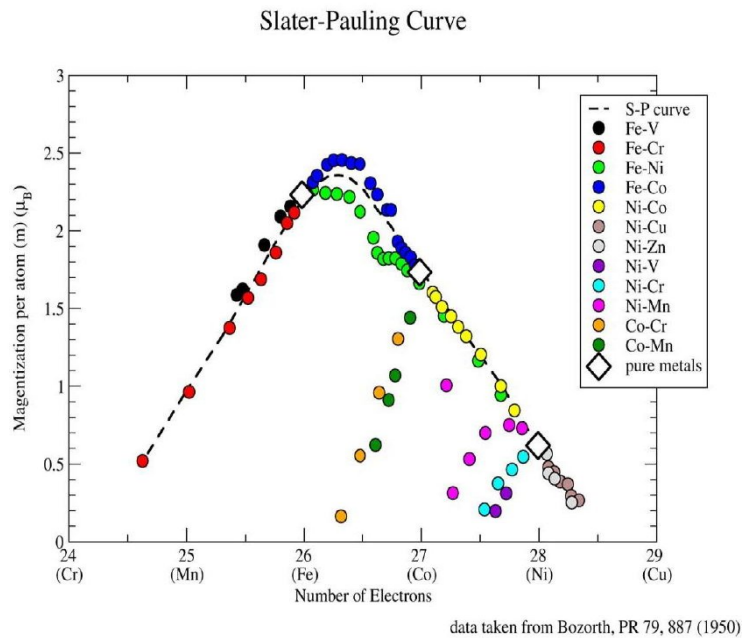


**Figure 1.** The Slater-Pauling Curve describes the systematic variation in the atomic magnetic moments (in units of  $\mu_B$ ), with respect to the number of electrons in the system (Podolak, et al. 2006).

Prior results using Fe/Pd and Co/Pd superlattices are mixed. X-ray magnetic circular dichroism (XMCD) and polarized neutron reflectivity (PNR) experiments have shown the development of an induced magnetic moment within the interfacial Pd (Awaji, et al. 2007; Bland, et al. 1995; Broeder, et al. 1987; Hillebrands, et al. 1988; Holmstrom, Nordstrom and Niklasson 2003). However, other experiments have shown a detrimental effect of laminating Pd with FeCo. Magnetically dead layers are introduced. These can extend several atomic layers into the ferromagnetic FeCo alloy (Bergmann 1978; Gyorgy, et al. 1980; Moodera and Meservey 1984). A Brillouin light scattering experiment with Pd strips shows no increase in the magnetic thickness of the sample. In other words, there is no induced moment in the Pd layers (Ackermann, et al. 2002).

For this thesis, we performed exploratory work using the Fe<sub>65</sub>Co<sub>35</sub> alloy as our ferromagnetic layer and Pd as our nonmagnetic layer. The samples were sputter-deposited at The University of Alabama. With subsequent characterization at The University of Alabama, the Synchrotron Radiation Center at the University of Wisconsin-Madison, and the Spallation Neutron Source at Oak Ridge National Laboratory. For comparison, we also deposited and characterized a FeCo/Ru superlattice of similar thickness. The choice of thickness results in the well-known antiferromagnetic coupling of the FeCo layers through the Ru layer (Parkin 1991).

## CHAPTER 2: EXPERIMENTS

Due to the limitations of the characterization techniques, two different types of samples were produced. XMCD has a limited probing depth (O'Brien and Tonner, Orbital and spin sum rules in x-ray magnetic circular dichroism 1994). Therefore, the samples for this experiment were single layers of the materials. These films consisted of 10 nm  $\text{Fe}_{65}\text{Co}_{35}$  ferromagnetic layer. On top of this, Pd was deposited. To look at the depth-dependence of the interfacial magnetic moments, films of zero, one, and two atomic layers (AL) of Pd were deposited. All four samples were grown directly on  $\sim 50$   $\text{mm}^2$  fused silica glass substrates, and capped with 2 nm of Al. The Al layer was allowed to naturally oxide, resulting in an approximately 3 nm Al-oxide capping layer.

Neutrons have a much higher probing depth than x-rays. For this experiment, a superlattice of 16 periods was grown. Silicon (1 0 0), with a 300 nm thick oxide layer, was used as the substrate; the substrates had an area of  $324 \text{ mm}^2$ . Each ferromagnetic layer consisted of 1.8 nm of  $\text{Fe}_{65}\text{Co}_{35}$ ; the nonmagnetic spacer layer consisted of 1.2 nm of either Pd or Ru. Five nanometers of Tantalum acted as the buffer layer between the substrate and the film, and as the capping layer to prevent oxidation. A third sample consisting of the Tantalum buffer, a ferromagnetic  $\text{Fe}_{65}\text{Co}_{35}$  layer, and 5 nm Ta capping layer was also deposited to set a baseline measurement.

All samples were grown in the Research and Analysis of Sputtering Conditions at Alabama (RASCAL) deposition apparatus. RASCAL is a home-designed and assembled ultra high vacuum system. The base pressure is  $3(10^{-7})$  Pa. The working gas is Argon

with a pressure of 0.36 Pa. Four confocal 1.5-inch magnetron sputtering guns, manufactured by AJA International, handle the deposition. Each gun can be used simultaneously for co-sputtering, or individually with computer-controlled shutters. A quartz microbalance determined the deposition rates of Fe<sub>65</sub>Co<sub>35</sub>, Pd, Ru, Ta, and Al at 0.02, 0.15, 0.03, 0.02, 0.017 nm/s, respectively. Each target used in the system has purity higher than 99.9 %.

After growth, the samples are subjected to multiple characterization techniques. For structural characterization, a Philips X'Pert MPD diffractometer with a Cu K- $\alpha$  radiation source was used for x-ray reflectivity (XRR) measurements. In the Philips diffractometer, the sample is placed vertically in the path of the x-ray beam. The film and x-ray tube are fixed, and the detector scans from approximately 0.5 degrees to 6 degrees. This glancing angle technique produces a reflectivity curve. This spectrum contains information on the film thickness, roughness, and density. Within the low angle range, phase information is not present. Figure 2 shows the typical geometry of an XRR experiment.

For a single-layer thick film, as shown in Figure 3, the analysis is quite simple. By determining the angular width of the oscillations, we can use the Bragg relation to determine the film thickness:

$$n\lambda = 2d \sin \theta \quad (1),$$

where  $n$  is the order of the diffraction (typically set to unity),  $d$  is the atomic spacing, and  $\theta$  is half the scattering angle. In the reflectivity experiment,  $d$  is the film thickness and  $\theta$  is the angular width of the oscillation. This is a result of the low angle and the chemical contrast present at the interface between two different materials.

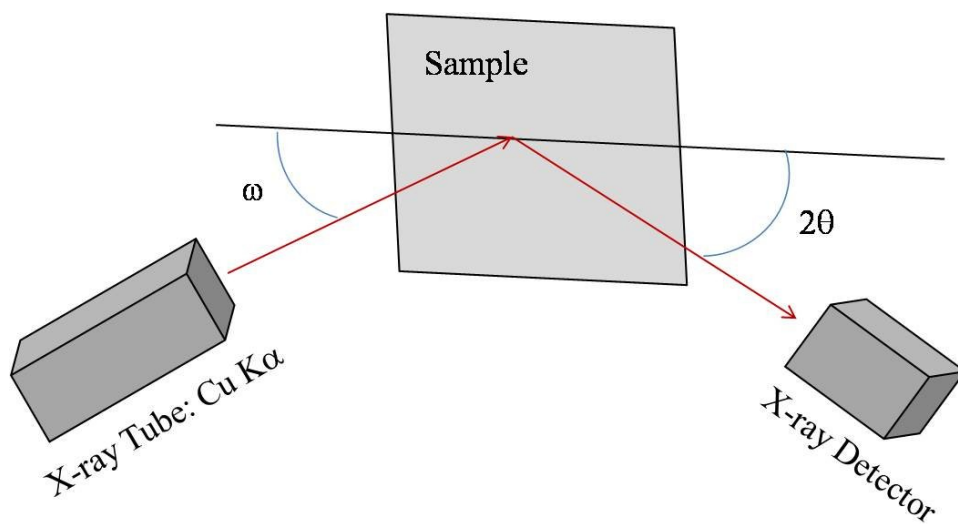


**Figure 2.** Typical geometry of an x-ray reflectivity (XRR) experiment.

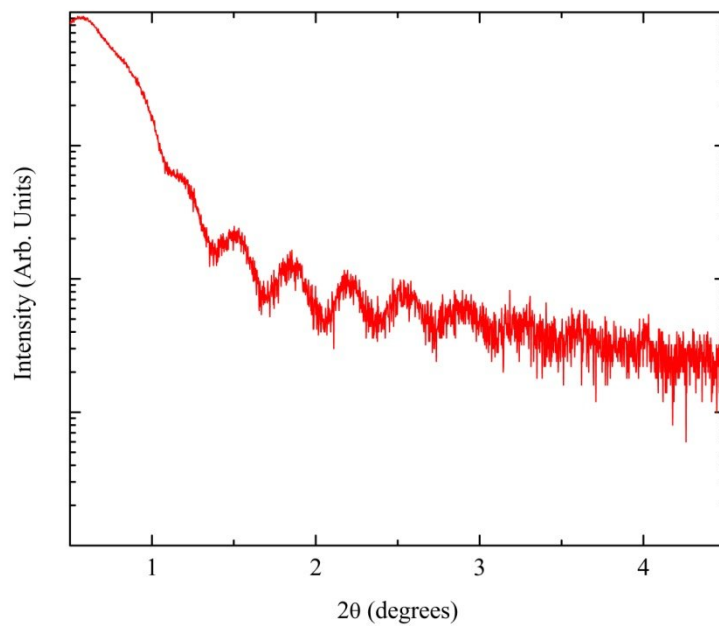


**Figure 3.** XRR curve of a single layer of  $\text{Fe}_{65}\text{Co}_{35}$ . The Bragg peak analysis technique leads to a film thickness of 24.5 nm. However, this does not provide any quantitative information on the chemical roughness of the sample.

However, for multilayer films, the presence of several elements, each with different atomic spacing, nullifies this approach. These spectra are fitted using the WinGIXA (de Boer and Leenaers 1996) software package. This package uses the Parratt recursive formalism (Parratt 1954), with a Névot-Croce error function (Nénot and Croce 1980) accounting for chemical roughness at the interfaces.

After the structural characterization is complete, we proceed to the magnetic characterization. The magnetic characterization was carried out via magneto-optical Kerr effect (MOKE) spectroscopy and vibrating sample magnetometry (VSM).

The MOKE spectrometer measures the change in the polarization state of linearly polarized light to determine the magnetic behavior of the sample. When linearly polarized light is incident upon a magnetic sample, the polarization state of the reflected beam has rotated with respect to the polarization direction of the incident beam. This Kerr rotation and its amplitude are proportional to the magnetization of the sample. If the magnetic field is parallel to the plane of incidence and perpendicular to the surface, the system is in polar configuration. This near normal incidence technique is sensitive to the magnetization vector component perpendicular to the surface. If the magnetic field is parallel to both the plane of incidence and the surface, the system is in a longitudinal setup. This is sensitive to the magnetization component parallel to both the surface and plane of incidence. If the magnetic field is normal to the incident plane and parallel to the surface, the system is transverse. This configuration is sensitive to the component parallel to the surface, but normal to the plane of incidence. Our spectrometer is limited to the longitudinal mode. Our setup is shown in Figure 4.

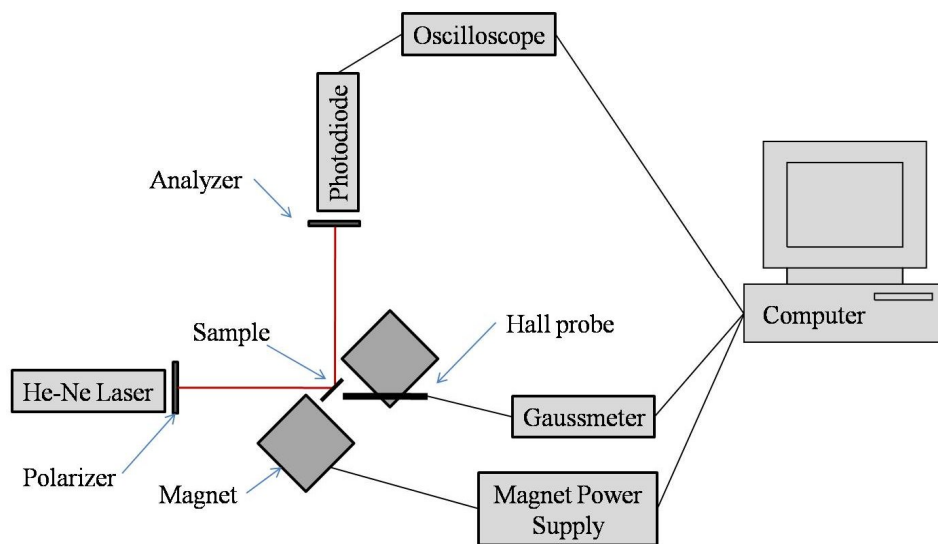


**Figure 4.** Typical arrangement for a magneto-optical Kerr effect (MOKE) spectrometer.

An intensity-stabilized, 10 mW Helium-Neon laser is linearly polarized. This light is incident upon the sample in a magnetic field, parallel to the surface and the plane of incidence. After reflection, an analyzer filters out the non-rotated light prior to collection by a sensitive photodiode. By sweeping the field through a user-defined range, we can generate a hysteresis curve. Unfortunately, the photodiode is limited to the collection of intensity data. This loss of the phase information limits our ability to compare the saturation magnetizations,  $M_s$  of different samples. However, this technique can accurately determine the saturation field,  $H_s$ , and coercive field,  $H_c$ , within a very short amount of time. All measurements were made at ambient temperature and pressure.

The samples designed for XMCD were sufficiently small to use the VSM. While the technique takes longer, more information about the overall sample magnetization can be obtained. The VSM utilizes Faraday's Law of Induction to measure the magnetic response of samples. An oscillating sample is placed in a static magnetic field, generating an electromagnetic signal that is measured by pickup coils, placed on the ends of the electromagnet. With the proper calibration, the pickup coil signal is converted to a magnetic measurement. To generate a hysteresis curve, this process is repeated over the course of a field sweep within the desired range. The result is a measurement of various magnetic parameters, such as the magnetic moment, the saturation field, and the coercive field. VSM measurements are limited by longer acquisition time and smaller samples, in comparison to MOKE. Another disadvantage of the VSM is its sensitivity to changes in the oscillation frequency and sample position. Any significant changes in these two areas will result in an error from the nominal value. Typically, these errors can be on the order

of a few per cent. Our measurements were performed at ambient temperature and pressure on a DMS Model 1660 VSM.

X-ray magnetic circular dichroism (XMCD) is a synchrotron radiation technique used to study the element-specific spin and orbital magnetic moments of ferromagnetic samples. This technique relies on the differential absorption cross-section of circularly polarized light, with respect to the spin orientation of the elemental electrons. By choosing the proper absorption edge, the observed dichroism in the spectra is a direct measure of the spin asymmetry, or magnetic moment, of a specific element within the sample. For the ferromagnetic transition metals, the magnetism is primarily mediated by the 3d-band electrons. As a result, the primary edges of interest are the  $L_3$  and  $L_2$  edges. The  $L_3$  edge is a transition of the  $3p_{3/2}$  core electrons to the 3d valence band; the  $L_2$  edge is the transition of the  $3p_{1/2}$  core electrons to the 3d valence band.

In the 4d noble metals, we suspect any interfacial moments would be due to a hybridization of the 3d and 4d bands. As a result, the ideal edges would still be the  $L_{3,2}$  transitions. However, the synchrotron source and beamline are limited in their range. Since the Pd  $L_3$  edge is eV, which is well beyond the maximum energy of 810 eV for the 10 m TGM, we are limited to studying the  $M_{3,2}$  edges. These are transitions from the core electrons to the core electrons.

Our measurements were conducted at ambient temperature in a custom-built, ultra-high vacuum chamber on the 10 m Toroidal Grating Monochromator (TGM) at the Synchrotron Radiation Center, the University of Wisconsin-Madison. The facility operates an 800 MeV electron storage ring, with user beam energy ranging from the

infrared to the soft x-ray regime. This particular beamline operates within the soft x-ray regime, with an energy range from 210 eV to 800 eV. At these energies, the typical escape depth of an electron is approximately 2 nm (O'Brien and Tonner, Surface-enhanced magnetic moment and ferromagnetic ordering of Mn ultrathin films on fcc Co(001) 1994).

Figure 5 shows the experimental setup, downstream from the toroidal grating monochromator. For our measurements, the polarity of the beam was kept constant. At each energy step, the sample is magnetized by a 0.14 T electromagnet; the magnet is turned off, and the total electron yield is collected by an analyzer held at 600 V. This process is repeated for the opposing magnetization.

The resulting spectra can be analyzed with the application of empirical sum rules (Thole, et al. 1992; Carra, et al. 1993; Lee, et al. 1997):

$$\frac{\langle L_z \rangle}{n_h} = -\frac{4}{3} \frac{q}{r P_{pol}} \quad (2)$$

$$\frac{\langle S_z \rangle - 7 \langle T_z \rangle}{n_h} = -\frac{6p - 4q}{r P_{pol}} \quad (3),$$

where  $\langle L_z \rangle$  is the orbital magnetic moment,  $\langle S_z \rangle$  is the spin magnetic moment,  $\langle T_z \rangle$  is the magnetic dipole term,  $n_h$  is the number of holes in the valence band,  $P_{pol}$  is the degree of polarization for the x-ray beam,

$$p = \int_{L_3} \sigma_M d\omega \quad q = \int_{L_3+L_2} \sigma_M d\omega \quad r = \int_{L_3+L_2} (\sigma^+ + \sigma^-) d\omega \quad (4),$$

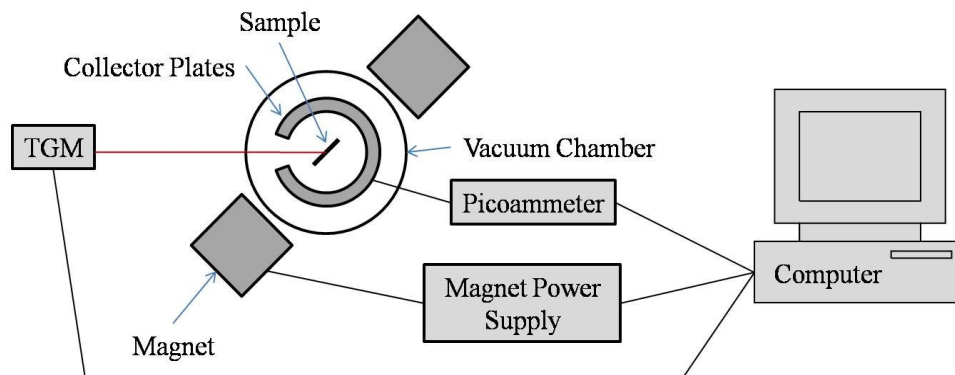


**Figure 5.** Typical set-up for a x-ray magnetic circular dichroism (XMCD) setup in total electron yield (TEY) mode.

where  $\sigma^+$  is the normalized x-ray absorption spectra (XAS) with the magnetization parallel to the direction of the photon spin,  $\sigma^-$  is the normalized XAS with the magnetization antiparallel to the direction of the photon spin, and  $\sigma_M$  is the difference between the normalized XAS signals. Unfortunately, the accuracy of this technique is limited to the 3d transition metals and it is dependent on precise knowledge of the beam polarization.

The beam polarization was recently measured with a 25 nm thermally evaporated Co film on a Si substrate, capped with 2.1 nm of Al. The measurement was performed at ambient temperature. The subsequent data is normalized to the sum of the two polarization states. These spectra are plotted in Figure 6.

Equations (2) and (3) are used to determine the beam polarization, assuming the magnetic dipole term,  $\langle T_z \rangle$  is negligible for systems with cubic symmetry (O'Brien and Tonner, Orbital and spin sum rules in x-ray magnetic circular dichroism 1994).

$$m = \langle L_z \rangle + 2\langle S_z \rangle \quad (5)$$

$$m = -\frac{4}{3} \frac{q}{rP_{pol}} - 2n_h \frac{6p - 4q}{rP_{pol}} \quad (6)$$

$$P_{pol} = -\frac{n_h}{mr \cos \theta} \left( 12p - \frac{20}{3}q \right) \quad (7).$$

The integrals  $p$ ,  $q$ , and  $r$  are determined experimentally from the data. The theoretical value of  $n_h$ , the number of holes in the valence band, is 2.1 for Co (Papaconstantopoulos 1986). The magnetic moment of bulk Cobalt is  $1.72\mu_B$ , at  $T = 0$  K (Kittel 1996).

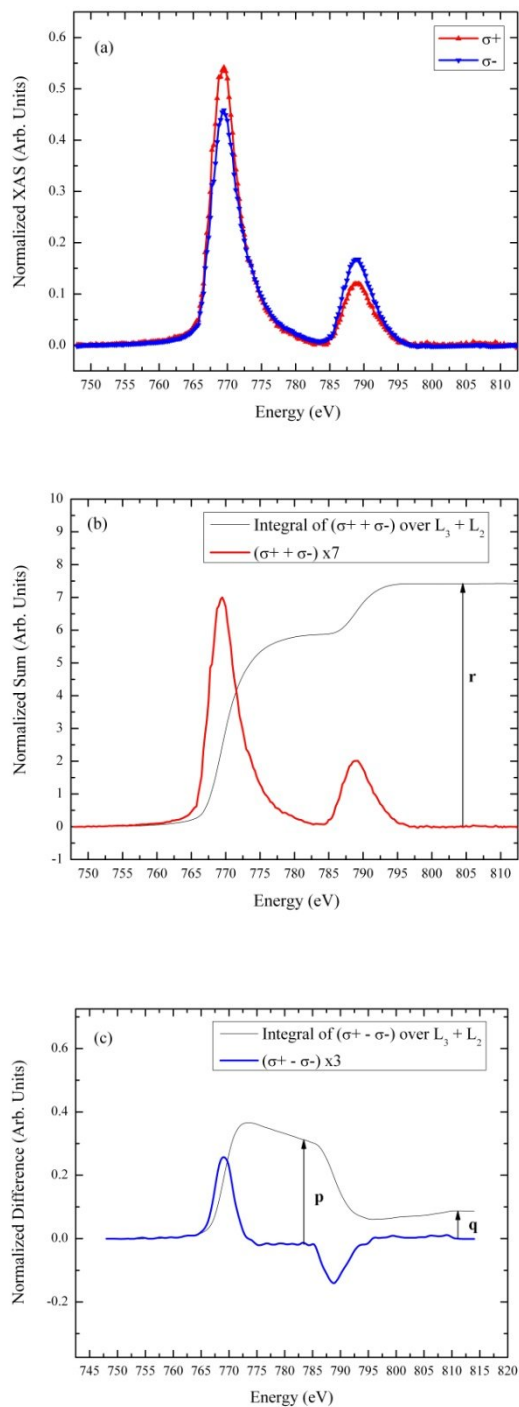


**Figure 6.** X-ray Magnetic Circular Dichroism (XMCD) spectra for the Co calibration sample. (a) shows the normalized x-ray absorption spectra for the two polarization states; (b) is the normalized sum of the two states; and (c) is the normalized difference spectra of the two spectra. The required integrals for the analysis are also shown.

However, the temperature dependence of the magnetization follows a phenomenological power law, with a critical exponent of  $\beta = 0.37 \pm 0.02$  (Krishnamurthy, et al. 2004):

$$\frac{M(T)}{M(0)} = \frac{m(T)}{m(0)} = \left(1 - \frac{T}{T_C}\right)^\beta \quad (8),$$

where  $M(T)$  is the magnetization at temperature  $T$ ,  $M(0)$  is the magnetization at absolute zero,  $m(T)$  is the magnetic moment at temperature  $T$ ,  $m(0)$  is the magnetic moment at absolute zero,  $T$  is the temperature of our measurement, and  $T_C$  is the Curie temperature. From this, we determine the room temperature magnetic moment of Cobalt is  $1.57\mu_B$ . The cosine term is the result of the experimental setup; our sample is placed at angle of 45 degrees, with respect to the beam path. The result is a beam polarization of  $(84 \pm 2)\%$  (Brauer, Pathak and LeClair 2009). The normalized values are not used in this calculation.

Polarized neutron reflectivity (PNR) is a complimentary technique to x-ray magnetic scattering. With the unique properties of the neutron, PNR is capable of determining the interfacial structure, magnetic roughness, and the distribution of the magnetization vector within multilayer samples (Zabel 2006). When looking at the geometries, PNR is very similar to x-ray reflectivity, Figure 7. The differences are the presence of a magnetic field and the use of neutrons. While both photons and neutrons are electrically neutral, neutrons possess a magnetic moment of  $1.913\mu_B$ . This electrical neutrality results in a significant probing depth, with sensitivity to magnetic materials, at significantly smaller energies than x-rays. Consequently, PNR spectra can provide similar information as XRR. However, in XRR, there is only information on the chemical structure. With a polarized neutron experiment, there is both chemical and magnetic

information. The major limit to neutron experiments are the relatively low fluxes involved, which results in long measurement times with relatively large samples.

As noted in Figure 7, a polarized neutron beam results in four possible scattering cross-sections:  $R^{++}$ ,  $R^{--}$ ,  $R^{+-}$ ,  $R^{-+}$ . The first superscript describes the incoming neutron polarization; the second superscript describes the scattered neutron polarization. Non-spin flip cross-sections ( $R^{++}$ ,  $R^{--}$ ) are sensitive to the magnetization vector parallel to the beam direction, resulting in a magnetic depth profile of the sample. Spin-flip cross sections ( $R^{+-}$ ,  $R^{-+}$ ) are sensitive to the magnetization vector perpendicular to the beam direction, yielding details on the magnetic nature of the sample surface. For this experiment, the samples are taken to beamline 4A at the Spallation Neutron Source. The vertical magnetism reflectometer has a resolution of approximately  $1.6(10^{-3})$  in  $Q_z$ , and  $1(10^{-7})$  in  $R$ . These high resolutions in both  $Q_z$  and  $R$ , with the addition of the higher fluxes available at the SNS, make it an ideal instrument for detecting small changes in the sample magnetization profile.

Our samples are placed under vacuum in a 0.05 T magnetic field. The non-spin flip cross-sections are measured at low temperature (5 K) and at room temperature (300 K), across three detector angles. The use of three angles is necessitated by the pulsed nature of the Spallation Neutron Source. For a continuous source of neutrons, such as the nuclear reactor at HFIR, there is a fixed wavelength, determined by the moderator on the particular beamline. At a pulsed source, there is a distribution of neutron speeds, i.e. wavelengths. As a result, there is the ability to conduct time of flight experiments. This opens the door to using neutrons to study spin dynamics. In addition to this, the use of an areal detector in combination with this distribution of wavelengths simplifies the

requirements of detector location. A full spectrum of the reflected angles can be obtained from only a few detector positions. The scattering angle is determined by their placement and time of arrival on the areal detector.

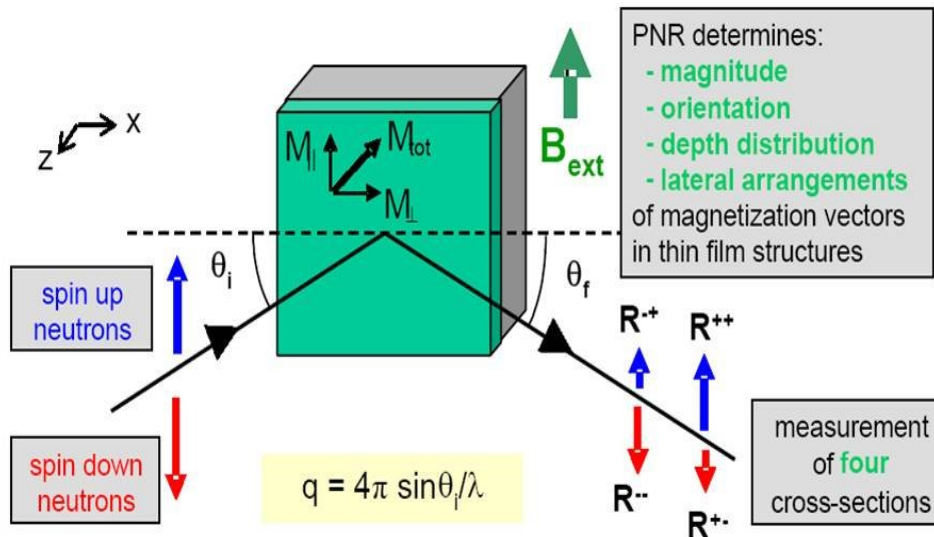


**Figure 7.** Polarized neutron reflectivity experiments result in four possible cross-sections (Ehlers and Klose 2006). The non-spin flip reflectivities yield information on the magnetic depth profile. The spin-flip cross-sections have information on the surface magnetism.

## CHAPTER 3: RESULTS AND DISCUSSION

### A. STRUCTURAL CHARACTERIZATION

Figure 8 shows the resultant spectra of the x-ray reflectivity measurement. A model of the sample is developed to account for the different scattering amplitudes of the various layers. This model is used in an iterative Parratt recursive formalism to account for the multilayer structure of the film, and a Névo-Croce error function formalism to account for the chemical roughness. The results of the fit show a superlattice period of 2.15 nm for the FeCo/Pd and 2.77 nm for the FeCo/Ru. This is approximately 28 % off the nominal value for the FeCo/Pd and about 8 % off the nominal value for the FeCo/Ru. There is a 25 % difference between the two superlattices.

The large error in the Pd superlattice may be due to the power during sputtering. When sputtering ferromagnetic materials, the requirement for stable, controlled plasma is approximately 10 % of the power supply output. For Pd, we used about 5 % of the power supply output. While this is sufficient for most normal metals, it may not have been for the Pd. Palladium has a magnetic susceptibility approximately 1 % of the ferromagnetic transition metals, but most normal metals are on the order of 0.1 % of the ferromagnetic transition metals. In other words, the stability of the sputtering yield may have been adversely affected by the lack of a stable power supply at low power.

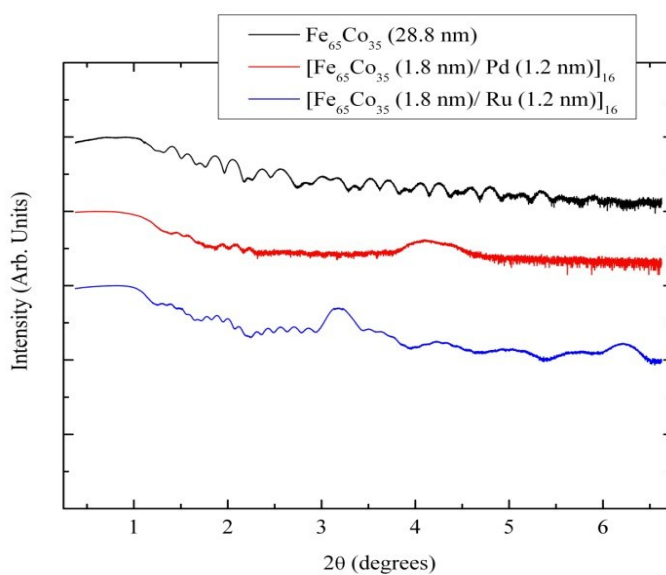


**Figure 8.** XRR spectra for the Fe<sub>65</sub>Co<sub>35</sub> baseline sample and the two superlattices used in the neutron experiment. The superlattices show Bragg peaks at 4.11 degrees for the FeCo/Pd and at 3.18 degrees for the FeCo/Ru.

## B. MAGNETIC CHARACTERIZATION: MOKE

The next step is magnetic characterization. Since the samples for the neutron are fairly large, the MOKE spectrometer is used to determine the saturation and the coercive fields of the easy axis. These values are summarized in Table 1, with the associated hysteresis curves shown in Figure 9.

With the introduction of nonmagnetic spacer layers, we see significant changes in the saturation fields, the coercivities and the squareness of the loops. With respect to the coercivity, there is a 32 % decrease with the introduction of Ru and a 112 % decrease with the introduction of Pd, compared to the  $\text{Fe}_{65}\text{Co}_{35}$  baseline sample. With the reduction in coercivity, we see a reduction in the area of the hysteresis. This corresponds to a reduction in the amount of energy lost during the magnetization process. In other words, the introduction of the spacer layers makes it easier to switch the magnetization. However, there are significant differences between the two spacer layers. For the Pd, the decrease is very large. This, coupled with the high amount of squareness in the loop, may indicate the values of the domain wall velocities are uniform, and/or any magnetization vector rotations within the domains are coherent.

With the Ru spacer layers, we see a slightly different picture. While there is a significant decrease in both the saturation field and the coercivity, we also see a 6 % decrease in the squareness of the loop. The reduction in the saturation field, and the coercivity, implies the sample magnetization is relatively easy to switch, but the decrease in the squareness of the loop indicates the layers may not all switch at the same time. This could be indicative of incoherent rotations, and/or a distribution of domain wall

velocities. In fact, the ferromagnetic layers may be weakly antiferromagnetically coupled. Further investigation by another technique is necessary to confirm this.

However, the end result is a complex magnetization process of both domain wall movement and domain magnetization rotation for the FeCo baseline, the FeCo/Pd and the FeCo/Ru samples (O'Handley 2000). Unfortunately, the lack of information on the value of the saturation magnetization,  $M_s$ , limits our quantitative analysis of this coercivity reduction.

**Table 1.** Summary of MOKE results.

Sample	Saturation Field, $H_S$ (kA/m)	Coercive Field, $H_C$ (kA/m)	Squareness, $M_r/M_s$
Si/SiOx/ Ta (5 nm)/ Fe <sub>65</sub> Co <sub>35</sub> (28.8 nm)/ Ta (5 nm)	$32.65 \pm 0.01$	$13.24 \pm 0.01$	$0.90 \pm 0.01$
Si/SiOx/ Ta (5 nm)/ Fe <sub>65</sub> Co <sub>35</sub> (1.8 nm)/ Pd (1.2 nm)/ Ta (5 nm)	$5.43 \pm 0.01$	$3.73 \pm 0.01$	$0.99 \pm 0.01$
Si/SiOx/ Ta (5 nm)/ Fe <sub>65</sub> Co <sub>35</sub> (1.8 nm)/ Ru (1.2 nm)/ Ta (5 nm)	$5.64 \pm 0.01$	$9.55 \pm 0.01$	$0.85 \pm 0.01$

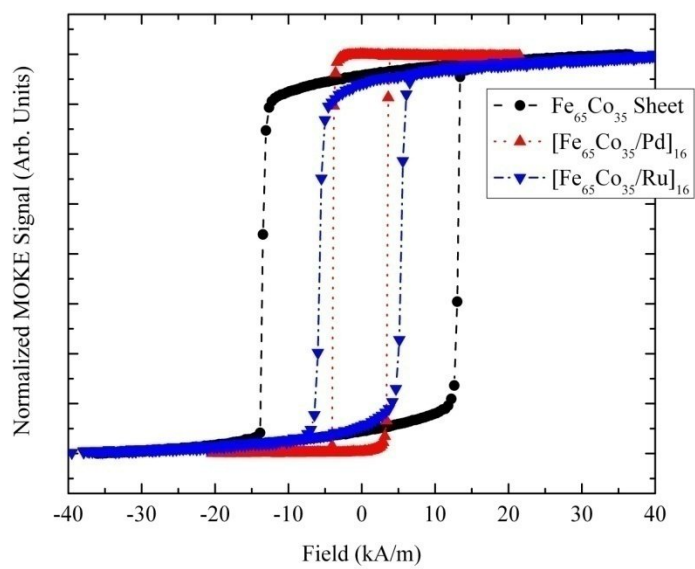


**Figure 9.** MOKE spectroscopy results on the Fe<sub>65</sub>Co<sub>35</sub> baseline sample and the two superlattices.

### C. MAGNETIC CHARACTERIZATION: VSM

While the MOKE is very useful, it does not give us a direct measurement with respect to the saturation magnetization of the sample. For this, we use the vibrating sample magnetometer (VSM). The VSM signal is a direct measurement of the overall magnetic moment of the sample. However, in order to compare two different samples, the magnetization of each needs to be calculated. The magnetization is

$$M = \frac{m}{V} \quad (9),$$

where  $M$  is the magnetization,  $m$  is the magnetic moment, and  $V$  is the magnetic volume of the sample.

To calculate the volume of our samples, we need the film thickness and the substrate area. Since the substrate size is not uniform, we use an optical scanning technique to determine the area. The completed samples are placed on an optical, flat-bed scanner. An image is taken; its size is measured with the use of Microsoft Windows Image Gallery. The result is an area with approximately 0.1 % statistical error. Traditional measurements result in larger errors (Wallock, et al. 2008).

The resultant magnetic volume calculation assumes that the entire volume of FeCo and Pd layers. With the optical scanning technique and the XRR fitting, we can determine the error in the volume calculation is approximately 5 %. With an assumed error of 0.5% in the magnetic moment values from the VSM, this leads to a magnetization error on the order of 6 %. The measured and calculated values are listed in Table 2. In inspecting the table and Figure 10, there is no significant change in the magnetization between the FeCo baseline and the FeCo/Pd (1 AL) samples.

**Table 2.** Summary of the VSM results for the XMCD samples. Please note,  $M_0$  is the saturation magnetization of the FeCo baseline sample.

Sample	Coercivity, $H_c$ (kA/m)	Saturation Field, $H_s$ (kA/m)	Saturation Magnetization, $M_s/M_0$	Squareness, $M_r/M_s$
FeCo baseline	$6.65 \pm 0.07$	$25.2 \pm 0.3$	1	$0.94 \pm 0.06$
FeCo/Pd (1 AL)	$6.96 \pm 0.07$	$19.9 \pm 0.2$	$0.951 \pm 0.007$	$0.93 \pm 0.07$
FeCo/Pd (2 AL)	$6.89 \pm 0.07$	$33.4 \pm 0.3$	$1.195 \pm 0.008$	$0.88 \pm 0.05$

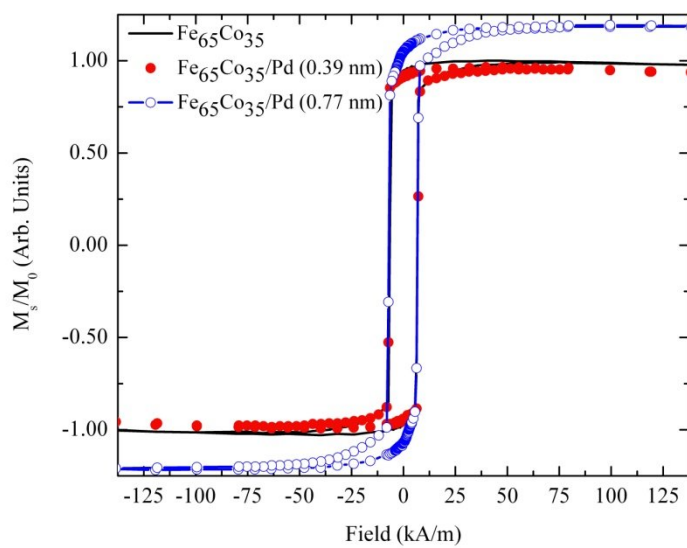


**Figure 10.** VSM results on the three XMCD samples. The saturation magnetization is normalized to the saturation magnetization of the FeCo baseline sample.

However, there is a significant change in the magnetization between the FeCo baseline and the FeCo/Pd (2AL) sample. This change is on the order of 17 % difference between the two values. It is possible that the observed differences are due to oxidation of the sample surface, which would be less pronounced in the sample with a greater thickness of Pd. However, we can gain understanding through a qualitative comparison of the samples.

The obvious conclusion is that Pd is affecting the magnetization process of the FeCo film. There are two possible reasons the Pd affects the magnetization process. One possibility is the addition of the Pd may have a pinning effect on domains near the interface. This would slow the magnetization process, which increases the coercivity and saturation fields. This would also support the reduction in squareness.

Another possibility is the prevention of oxidation. If the Al capping layer was fully oxidized, oxygen would have access to the magnetic layer. This would lower the overall magnetization of the sample. Assuming this is the case, we note that a single atomic layer of Pd is insufficient to block the oxidization of the  $\text{Fe}_{65}\text{Co}_{35}$  alloy. However, the introduction of a second AL of Pd is sufficient to block the oxidation of the  $\text{Fe}_{65}\text{Co}_{35}$  alloy.

## D: X-RAY MAGNETIC CIRCULAR DICHROISM

In applying the sum rules to our data, we make several key assumptions. The first is with respect to the magnetic dipole term. Our materials have primarily cubic symmetry. This results in the cancellation of dipole interactions over the summation of the cubic crystal (O'Handley 2000). As a result, the magnetic dipole term is negligible in Equation (3) (O'Brien and Tonner, Orbital and spin sum rules in x-ray magnetic circular dichroism 1994). Our other assumption is the number of holes in the valence band. We use the theoretical values of 3.1 for Fe and 2.1 for Co (Papaconstantopoulus 1986). With these constraints in mind, the spectra of the FeCo baseline sample are plotted in Figure 11; the results of the XMCD analysis are summarized in Table 4.

By inspection of the analysis results in Table 4, we note a definite decrease in the overall magnetic moments of the Co, with increasing Pd thickness. The Fe moments show no trend. They are statistically equivalent for all three samples. However, both elements show a decrease in the ratio of the orbital to spin moments, with increasing Pd thickness. In breaking down this trend, we note slightly different results for the two elements. In the Fe, the spin moments are relatively stable and unaffected by the introduction of Pd. The resulting decrease in the ratio is mainly due to the orbital moments. For Co, both the spin and orbital moments are decreasing with increased Pd content. Unfortunately, this data does not agree with our VSM data. Both the Fe and Co edges show decreased moments with the introduction of Pd. This can be summarized in Figure 12, which shows a steady decrease in the dichroism signal with increasing Pd content.

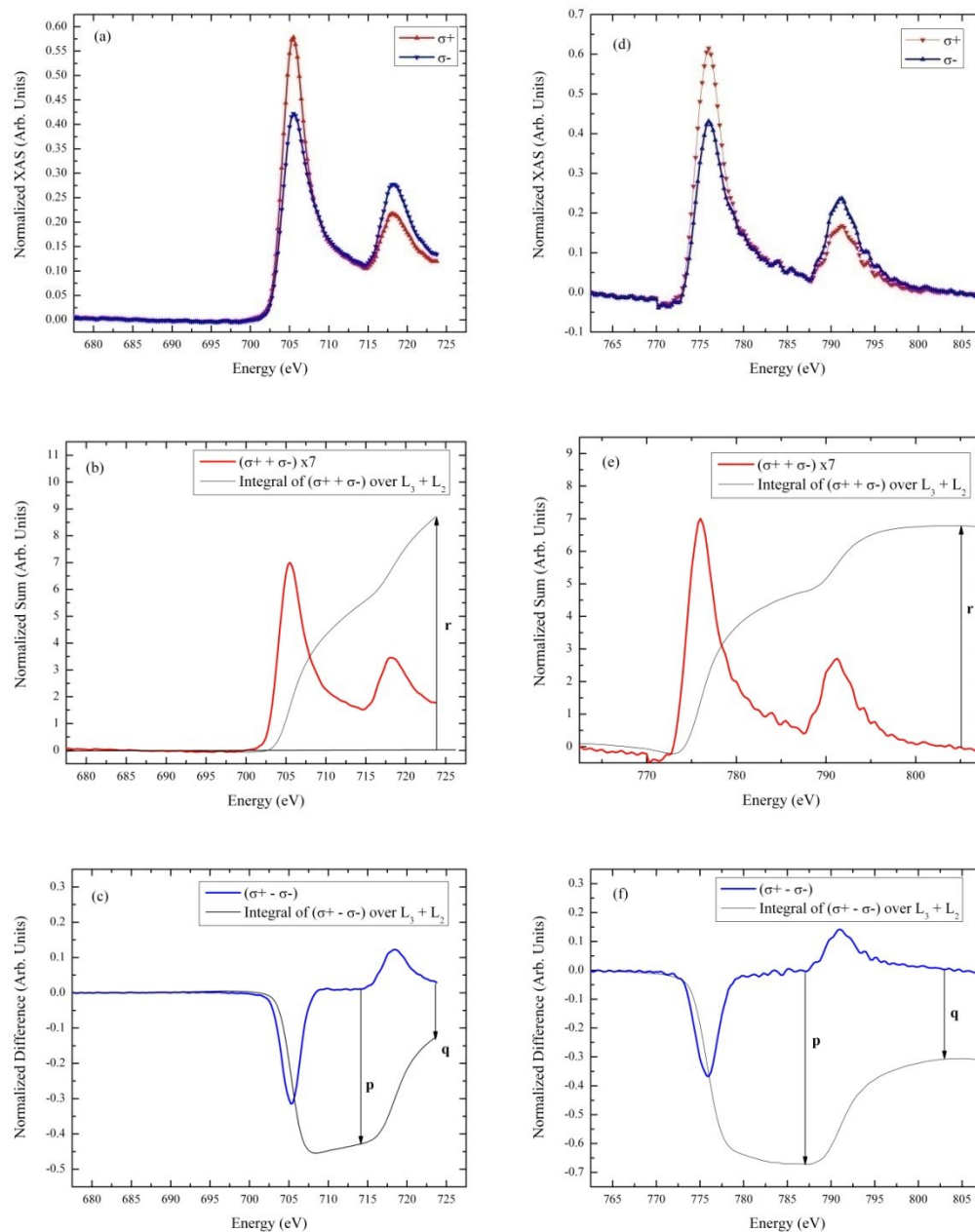


**Figure 11.** X-ray Magnetic Circular Dichroism (XMCD) spectra for the FeCo baseline sample. With respect to the Fe edges, (a) shows the normalized x-ray absorption spectra for the two polarization states; (b) is the normalized sum of the two states; and (c) is the normalized difference spectra of the two spectra. The same are shown for the Co edges in (d) to (f). The required integrals for the analysis are also shown.

**Table 3.** Summary of XMCD results for the calculated magnetic moments. All measurements are in units of  $\mu_B$ .

Sample		Fe		Co	
		Component	Ratio $\langle L_z \rangle / \langle S_z \rangle$	Component	Ratio $\langle L_z \rangle / \langle S_z \rangle$
FeCo baseline	$\langle L_z \rangle$	$0.066 \pm 0.004$	$0.078 \pm 0.001$	$0.144 \pm 0.006$	$0.145 \pm 0.001$
	$\langle S_z \rangle$	$0.89 \pm 0.04$		$0.99 \pm 0.03$	
	m	$1.85 \pm 0.15$		$2.12 \pm 0.13$	
FeCo/Pd (1 AL)	$\langle L_z \rangle$	$0.053 \pm 0.004$	$0.061 \pm 0.001$	$0.066 \pm 0.005$	$0.074 \pm 0.002$
	$\langle S_z \rangle$	$0.89 \pm 0.03$		$0.89 \pm 0.02$	
	m	$1.83 \pm 0.11$		$1.85 \pm 0.07$	
FeCo/Pd (2 AL)	$\langle L_z \rangle$	$0.018 \pm 0.004$	$0.019 \pm 0.001$	$0.012 \pm 0.002$	$0.019 \pm 0.001$
	$\langle S_z \rangle$	$0.95 \pm 0.04$		$0.64 \pm 0.02$	
	m	$1.91 \pm 0.15$		$1.30 \pm 0.04$	

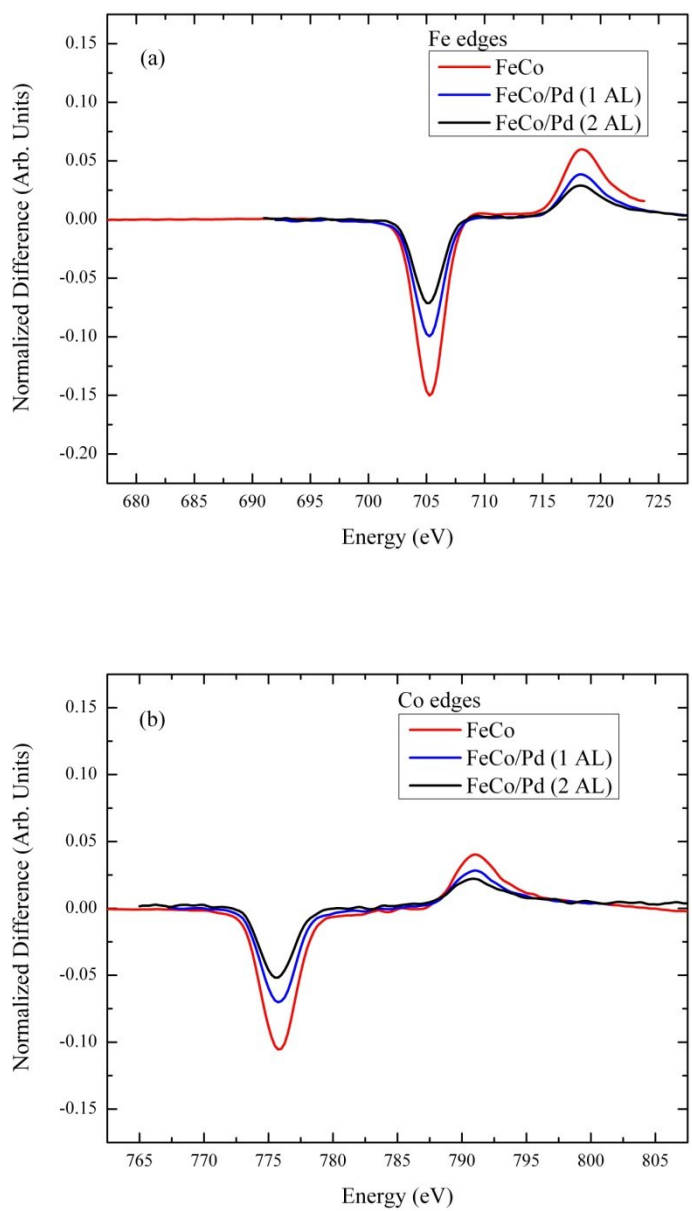


**Figure 12.** Comparison of the difference spectra for (a) the Fe edges and (b) the Co edges in the three samples.

While the examination of XMCD data is quite straightforward for the 3d transition metals, there are some problems that may not be accounted for in this analysis. One such quandary is the number of holes for the material. In bulk, single element materials, the theoretical values used are accepted. However, in FeCo alloys, there is hybridization of the Fe and Co valence bands (MacLaren, et al. 1999). As a result, the number of Fe holes may actually decrease, and the Co holes increase. If this varied by 0.25 holes for Fe, it would increase the amount of error by an order of magnitude! The polarization is another issue. It is calculated from the sum rules, using the theoretical values of the valence band holes for Co. While the calibration sample was a relatively thick Co layer, and the resulting polarization is within the expected regime, the value has not been verified by an independent method.

Using the ratio of the orbital to spin magnetic moments is a good approach to alleviating these two problems. The calculated ratio, as shown below, cancels out both the polarization and the number of holes in the valence band.

$$\frac{\langle L_z \rangle}{\langle S_z \rangle} = \frac{-\frac{4}{3} \frac{q}{rP_{pol}}}{-n_h \frac{(6p-4q)}{rP_{pol}}} = \frac{4}{3} \frac{q}{6p-4q} \quad (10),$$

where  $q$  is the integral of the difference in the  $L_{3,2}$  peaks and  $p$  is the integral of the difference in the  $L_3$  peak. Consequently, this value is free from the errors in polarization and valence holes. For example, tetragonal distortion of the FeCo leads to an enhancement of the orbital magnetic moment (Yildiz, et al. 2008). In comparing our data to their “upper” limits, we see all our numbers are well within the range allowed.

While the orbital to spin ratio is free from the errors in the polarization and the valence band holes, oxidation plays a significant role. Looking at Figures 15(a) and (d),

we can see the overlap of the  $L_3$  and  $L_2$  peaks. For the Fe edges, this occurs over the energy range of 708 to 715 eV; for Co, this occurs from 780 to 787 eV. This overlap is primarily due to oxidation states of the Fe and Co, respectively. Since the emitted electrons have an escape depth of only a few nanometers, this oxidation has a significant effect in total electron yield mode. As for the analysis, this leads to an overestimation in the integral  $r$ , and an underestimation in the integral  $q$ . These values play significant roles in the analysis of the spectra, leading to the significant differences between our calculated values and the accepted moments for the materials.

Another issue we cannot account for is sample charging. With using glass substrates, there is no electrical contact between the samples and the instrument ground. As a result, a static charge builds up on the sample surface. As shown in the energy range of 798 to 810 eV, in the Co spectra of Figures 15(d) and (f). As the static charge builds on the sample, there is a progressive reduction in the count rate of the total electron yield over the course of the experiment. This could result in a reduction of the dichroism signal at either, or both, the  $L_3$  and  $L_2$  peaks; this leads to unknown errors in the magnetic moment calculations.

To alleviate the problems associated with surface-sensitive techniques, we developed superlattice structures to study using polarized neutrons, which integrate over the entire sample. The non-spin flip channels are insensitive to surface effects, yielding both the chemical and magnetic depth profiles of the samples. The superlattice structure will also allow the investigation of lattice expansion effects in the ferromagnetic material. Since the Pd was located above the FeCo in the XMCD sample stack, there is no induced

strain in the FeCo layer. However, with the repeating bilayer structure of a superlattice, there is induced strain in the FeCo layers.

## E: POLARIZED NEUTRON REFLECTIVITY

For the PNR experiment, we took two superlattice samples to Beamline 4A (Vertical Magnetism Reflectometer) at the Spallation Neutron Source. Each sample was placed under vacuum to facilitate temperature control of the samples. Two measurements for each sample were taken over the course of 4 days. Each measurement consisted of 3 detector angle positions, with the sample in a 0.05 T magnetic field. The temperature was 300 K for room temperature run, and set at 5 K for the low temperature run. The resulting curves are plotted in Figure 13. In looking at the neutron data, we see the clear splitting in the FeCo/Pd sample, but no definitive Bragg peaks. With the FeCo/Ru sample, we see a clear lack of splitting and a definitive Bragg peak at  $0.11 \text{ \AA}^{-1}$ .

Fitting polarized neutron data is an iterative process. One way to begin is with a simple analogy from light optics. In optical scattering, the critical angle is the transition point between a purely effervescent wave and a real wave travelling within the sample; the transition between total internal reflection and normal scattering. In light optics, Snell's law provides the basis between the relationship of the index of refraction and the critical angle,

$$\sin \theta_c = \frac{n_2}{n_1} \quad (11),$$

where  $\theta_c$  is the critical angle for total internal reflection,  $n_1$  is the index of refraction for the medium above the surface of the material, and  $n_2$  is the index of refraction for the material. In photon optics, the index of refraction is related to the scattering amplitudes of the component materials:

$$n = 1 - \frac{r_e}{2\pi} \lambda^2 \sum_j N_j (f_{j1} + if_{j2}) \quad (12),$$

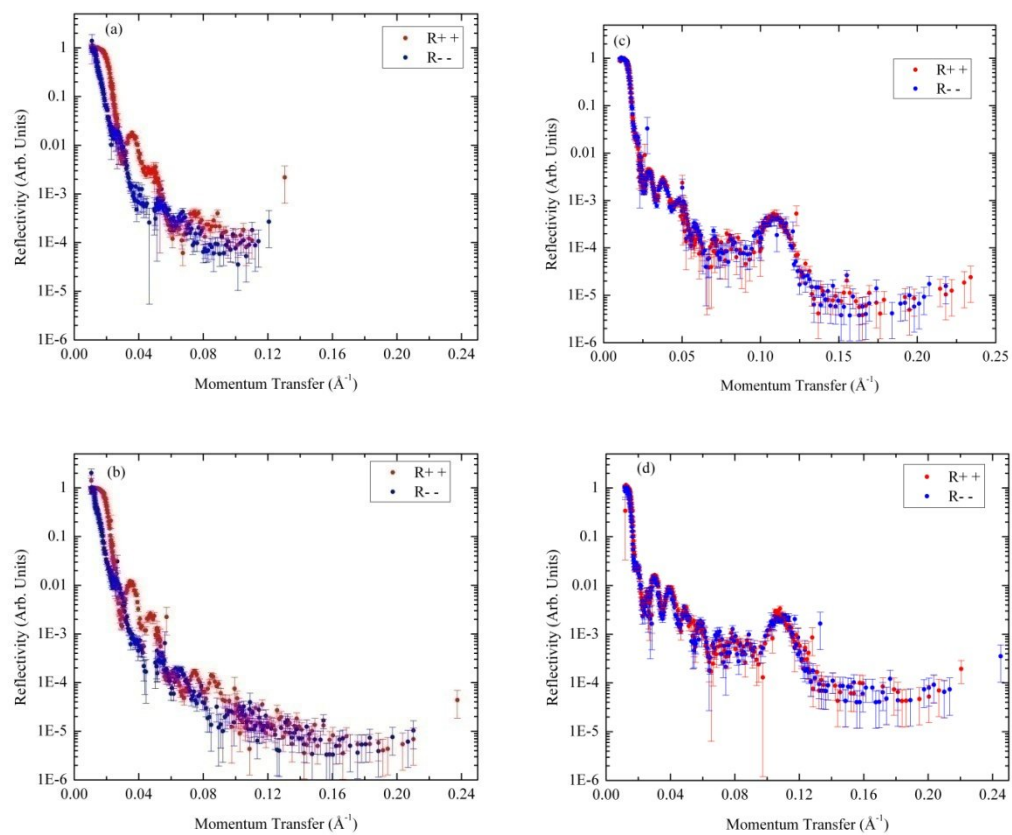


**Figure 13.** The non-spin flip reflectivities for the FeCo/Pd at (a)  $T = 5$  K, at (b)  $T = 300$  K, the FeCo/Ru (c) at  $T = 5$  K, and (d) at  $T = 300$  K.

where  $r_e$  is the classical electron radius,  $\lambda$  is the wavelength of the light,  $N_j$  is the number of atoms of type  $j$  per unit volume,  $f_{j1}$  is the real part of the atomic scattering factor for atoms of type  $j$ , and  $f_{j2}$  is the imaginary part of the atomic scattering factor for atoms of type  $j$  (Gullikson 2001). In photon optics, this generally results in a value greater than unity. This leads us to total internal reflection for the material.

For neutron optics, we can make a similar statement with respect to the nuclear and magnetic scattering lengths,

$$n = 1 - kN(b_n \pm b_m) \quad (13),$$

where  $k$  is a constant defined by the material properties,  $N$  is the number density of the material,  $b_n$  is the neutron nuclear scattering length, and  $b_m$  is the neutron magnetic scattering length (National Institute of Standards and Technology 1998). This value is typically less than unity for neutron optics. Therefore, instead of the total *internal* reflection of photon optics, neutrons undergo total *external* reflection (King 2003).

Therefore, we can relate the position of the critical angle to the scattering length of the incident neutrons,

$$\sin \theta_c = n_2 = 1 - kN(b_n \pm b_m) \quad (14).$$

However, one thing to note, neutron experiments are typically measured in momentum space rather than real space. Therefore, we need to convert our critical angle to a critical edge:

$$Q_c = \frac{4\pi}{\lambda} \sin \theta_c \quad (15)$$

where  $Q_c$  is the momentum transfer at the critical edge,  $\lambda$  is the neutron wavelength,  $q_c$  is the critical angle in radians. Therefore, our relationship of the critical edge to the neutron scattering lengths becomes,

$$\sin\left(\arcsin\left(\frac{\lambda}{4\pi}Q_c\right)\right) = n = 1 - kN((b_n \pm b_m)) \quad (16)$$

$$Q_c = \frac{4\pi}{\lambda} [1 - kN(b_n \pm b_m)] \quad (17).$$

The use of a polarized neutron beam results in four possible reflectivity cross-sections, each with its own critical edge. Using the difference in the critical edges of the non-spin flip cross-sections ( $R^{++}$ ,  $R^{--}$ ), we can gain insight into the bulk behavior of the sample.

$$\Delta Q_c = Q_c^{++} - Q_c^{--} = \frac{4\pi}{\lambda} [1 - kN(b_n + b_m)] - \frac{4\pi}{\lambda} [1 - kN(b_n - b_m)] \quad (18)$$

$$\Delta Q_c = -2 \frac{4\pi}{\lambda} kN b_m \quad (19).$$

For magnetic scattering, the scattering length can be linked to the magnetic moment through a magnetic scattering length density,

$$\delta_m = b_m \frac{\rho N_A}{M_m} = \frac{Cm}{V} \quad (20),$$

where  $\delta_m$  is the magnetic scattering length density,  $b_m$  is the magnetic scattering length,  $\rho$  is the bulk mass density,  $N_A$  is Avogadro's number,  $M_m$  is the molar mass,  $C$  is a constant ( $C = 2.645(10^{-5}) \text{ \AA}/\mu_B$ ),  $m$  is the magnetic moment in units of  $\mu_B$ , and  $V$  is the volume of the molecule (Fitzsimmons and Majkrzak 2005). From this, we see the magnetic scattering length is directly proportional to the magnetic moment of the molecule. When looking at the critical edge, we are looking at the bulk-like behavior of the sample. In

other words, the splitting of the critical edge is directly proportional to the “bulk” magnetic moment of the sample,

$$\Delta Q_c = -\frac{8\pi}{\lambda} kNCm = A_{material}m \quad (21),$$

where  $A_{material}$  is a constant of proportionality containing information on the materials and their interactions with each other,  $m$  is the “bulk” magnetic moment of the sample.

In Figure 14(a) and 14(b) are the critical edges for the FeCo/Pd and FeCo/Ru superlattice samples. By inspection, we see the splitting between the critical edges of the FeCo/Pd samples are much larger than the splitting between the FeCo/Ru edges. By our simple analogy, the magnetic moment of the FeCo/Pd is larger than the magnetic moment of the FeCo/Ru sample. When looking at the FeCo/Pd sample, we see the splitting at room temperature is  $0.0658 \text{ \AA}^{-1}$ ; for the low temperature measurement, the splitting increases to  $0.0657 \text{ \AA}^{-1}$ . The instrument resolution is  $0.0016$ , assuming the mean wavelength is  $4 \text{ \AA}$  (Klose 2000). There is no real difference between the room temperature splitting and the low temperature splitting. This is unexpected. From Equation (8), our phenomenological power law for the temperature dependence of the magnetization, we would expect to see a 8 % increase in the splitting between the room temperature and low temperature measurements; we assume a Curie temperature of approximately 1500 K (MacLaren, et al. 1999). In the FeCo/Ru system, the splitting is  $\Delta Q_c = 0.00044 \text{ \AA}^{-1}$  at room temperature, and  $\Delta Q_c = 0.00019 \text{ \AA}^{-1}$  at low temperature. In both cases, this is less than the resolution of the instrument.

This current analysis does not seem to lend itself to any definite conclusion. Further analysis of the complete spectra, using the proper software, is necessary to fully understand what is happening in the FeCo/Pd and FeCo/Ru systems.

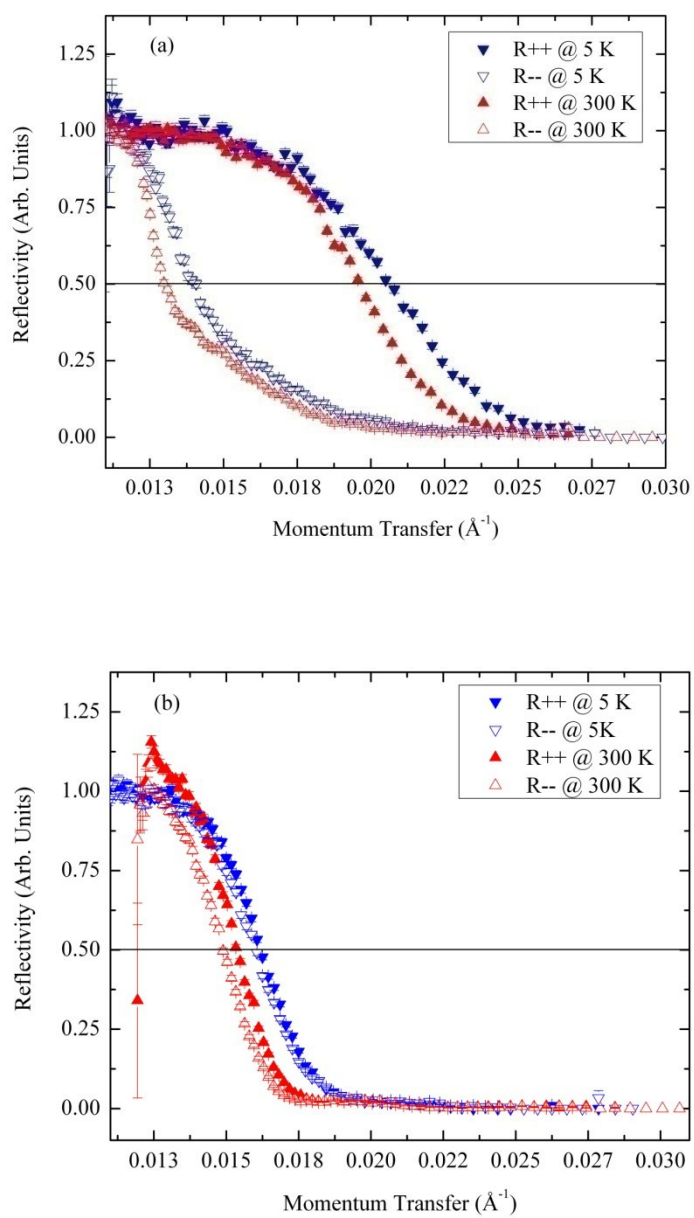


**Figure 14.** The reflectivities near the critical edge for the (a) FeCo/Pd and (b) the FeCo/Ru. The red indicates room temperature, the blue indicates low temperature.

## CONCLUSIONS

We have used several techniques to study the interfacial interactions of  $\text{Fe}_{65}\text{Co}_{35}$  with Pd. From our x-ray reflectivity data, we determine the superlattice periodicity of the FeCo/Pd multilayers to be significantly off the nominal target. We suspect this is due to the instability of the sputtering power supply at low power, leading to instability in the sputtering yield. In future work, we will adjust the power supply to the requisite rule of thumb, 10 % of the output, for ferromagnetic materials.

However, despite this problem, we were successful in creating magnetic superlattices, as evidenced by both the x-ray reflectivity and the magneto-optical Kerr effect (MOKE) spectra. The MOKE spectra show a significant change in the magnetic characteristics of the film with the introduction of the non-magnetic spacer layers, Ru and Pd. The Pd superlattice showed a significant reduction in coercivity and an increase in the loop squareness. Both of these trends are indicative of a lower amount of energy loss during the magnetization process. In the Ru sample, there was also a significant reduction in coercivity, but the loop squareness was less than the baseline sample. Clearly, there is a more complex process for this system compared to the Pd sample.

For our x-ray magnetic circular dichroism (XMCD) experiment, we developed FeCo films with a varying amount of Pd atomic layers (AL) deposited on the surface. The vibrating sample magnetometer (VSM) data show a lack of change between the FeCo baseline and the FeCo/Pd (1 AL) sample. The FeCo/Pd (2 AL) samples shows a large increase in the magnetization. This is a result of oxidation in the FeCo. The

single atomic layer of Pd was insufficient to protect the FeCo from the oxygen which “seeped” through the Al capping layer. The FeCo/Pd (2 AL) sample has sufficient Pd to protect the FeCo from oxidation. However, this cannot be confirmed by our XMCD data. The XMCD data shows an across the board decrease in the magnetic moments of the Fe and Co atoms in the samples, as the Pd thickness is increased. While we may not completely trust the calculated values, the trend is clear. It is possible the introduction of Pd increases the surface roughness. This, along with oxidation, will decrease the observed magnetic moments.

In the polarized neutron reflectivity experiments, we measured two superlattice samples, and are in the process of completing the fitting process. In our initial fitting procedure, we used a simple optical analogy to analyze information near the critical edge. While the FeCo/Pd superlattices showed significant splitting, there was a decided lack of change between the low and room temperature measurements. Preliminary fitting, using the Parratt software package, shows that the splitting could be caused by a magnetic moment of approximately  $2.3\mu_B/\text{atom}$ . This is within the expected range of the  $\text{Fe}_{65}\text{Co}_{35}$  system. However, a more complete analysis is necessary to confirm this. In the FeCo/Ru system, there was a complete lack of splitting at both low and room temperature. This trend seems to continue throughout the entire spectra. A more complete analysis, using the Parratt32 software, is necessary to determine the full extent of the interfacial interactions in both the FeCo/Ru and FeCo/Pd systems.

## BIBLIOGRAPHY

- Ackermann, J. J., I. Guedes, C. Leighton, M. Grimsditch, and I. K. Schuller. "Upper bound for the magnetic proximity effect extracted from Brillouin light scattering." *Physical Review B* 65 (2002): 104432.
- Awaji, N., et al. "Soft X-ray Resonant Magnetic Reflectivity Study on Induced." *Journal of Physics: Conference Series*. 2007. 012034.
- Bergmann, G. "Transition from Pauli Paramagnetism to Band Ferromagnetism in Very Thin Ni Films." *Physical Review Letters* 41 (1978): 264.
- Bland, J. A.C., C. Daboo, B. Heinrich, Z. Celinski, and R. D. Bateson. "Enhanced magnetic moments in bcc Fe films." *Physical Review B* 51 (1995): 258.
- Brauer, J., M. Pathak, and P. LeClair. 2009.
- Broeder, F. J. A., H. C. Donkerslott, H. J. G. Draaisma, and W. J. M. de Jonge. "Magnetic properties and structure of Pd/Co and Pd/Fe multilayers." *Journal of Applied Physics* 61 (1987): 4317.
- Carra, P., B. T. Thole, M. Altarelli, and X. Wang. "X-ray Circular Dichroism and Local Magnetic Fields." *Physical Review Letters* 70 (1993): 694-697.
- de Boer, D. K. G., and A. J. G. Leenaers. "WinGIXA simulation software." Eindhoven: Philips Analytical, 1996.
- Ehlers, G., and F. R. Klose. *Characterization of Magnetic Materials by Means of Neutron Scattering*. Vol. 2, in *Handbook of Advanced Magnetic Materials, Characterization and Simulation*, edited by Y. Liu, D. J. Sellmyer and D. Shindo, 66-112. New York: Springer, 2006.
- Fitzsimmons, M. R., and C. F. Majkrzak. "Application of polarized neutron reflectometry to studies of artificially structured magnetic materials." In *Modern techniques for characterizing magnetic materials*, edited by Y. Zhu, 107-155. Boston, MA: Kluwer Academic Publishers, 2005.
- Fu, Y., X. Cheng, and Z. Yang. "Soft magnetic properties and microstructure of Fe<sub>65</sub>Co<sub>35</sub> thin films with different underlayers." *Physica Status Solidi (A)* 203, no. 5 (2006): 963-969.

- Gullikson, E. M. "Atomic Scattering Factors." In *X-ray Data Booklet*, by A. C. Thompson, et al., edited by A. C. Thompson and D. Vaughan, 1.44-1.53. Berkeley, CA: Lawrence Berkeley National Laboratory, 2001.
- Gyorgy, E. M., J. F. Dillon, D. B. McWhan, L. W. Rupp, L. R. Testardi, and P. J. Flanders. "Magnetic Properties of Compositionally Modulated Cu-Ni Thin Films." *Physical Review Letters* 45 (1980): 57.
- Hillebrands, B., et al. "Brillouin scattering from collective spin waves in magnetic superlattices." *Journal of Applied Physics*, no. 63 (1988): 3880.
- Holmstrom, E., L. Nordstrom, and A. M. N. Niklasson. "Giant magnetic enhancement in Fe/Pd films and its influence on the magnetic interlayer coupling." *Physical Review B* 67 (2003): 184403.
- King, S. M. "Introduction to Small Angle Neutron Scattering." Large-scale Structures Group. September 2003. <http://www.isis.rl.ac.uk/largescale/loq/documents/sans.htm> (accessed March 19, 2009).
- Kittel, C. *Introduction to Solid State Physics*. 7th. New York: John Wiley & Sons, Inc, 1996.
- Klose, F. R. *Design Criteria for the Spallation Neutron Source Instrument Systems Magnetism Reflectometer*. Spallation Neutron Source, Oak Ridge National Laboratory, Oak Ridge, TN: UT-Batelle, Inc., 2000.
- Krishnamurthy, V. V., et al. "Antiferromagnetic phase transitions in an ordered Pt<sub>3</sub>Fe(111) film studied by neutron diffraction." *Physical Review B* 70 (2004): 024424.
- Lee, J., et al. "A direct test of x-ray magnetic circular dichroism sum rules for strained Ni films using polarized neutron reflection." *Journal of Physics: Condensed Matter* 9 (1997): L137-L143.
- MacLaren, J. M., T. C. Schulthess, W. H. Butler, R. Sutton, and M. McHenry. "Electronic structure, exchange interactions, and Curie temperature of FeCo." *Journal of Applied Physics* 85 (1999): 4833-4835.
- Moodera, J. S., and R. Meservey. "Magnetic proximity effect in thin films of Ni on nonmagnetic metals." *Physical Review B* 29 (1984): 2943.
- National Institute of Standards and Technology. "The neutron index of refraction." *NIST Ionizing Radiation Division*. November 1998. <http://physics.nist.gov/Divisions/Div846/Gp3/NIOF/web04c.html> (accessed March 16, 2009).

- Névot, L., and P. Croce. "Caractérisation des surfaces par réflexion rasante de rayons X. Application à l'étude du polissage de quelques verres silicates." *Revue de Physique Appliquée* 15 (1980): 761.
- O'Brien, W. L., and B. P. Tonner. "Orbital and spin sum rules in x-ray magnetic circular dichroism." *Physical Review B* 50 (1994): 12672.
- O'Brien, W. L., and B. P. Tonner. "Surface-enhanced magnetic moment and ferromagnetic ordering of Mn ultrathin films on fcc Co(001)." *Physical Review B* 50 (1994): 2963-2969.
- O'Handley, R. C. *Modern Magnetic Materials: Principles and Applications*. New York: John Wiley & Sons, 2000.
- Papaconstantopoulus, D. A. *Handbook of the Band Structure of Elemental Solids*. New York: Plenum, 1986.
- Parkin, S. S. P. "Systematic variation of the strength and oscillation period of indirect magnetic exchange coupling through the 3d, 4d, and 5d transition metals." *Physical Review Letters* 67 (1991): 3598.
- Parratt, L. G. "Surface Studies of Solids by Total Reflection of X-Rays." *Physical Review* 95 (1954): 359.
- Pauling, Linus. "The Nature of the Interatomic Forces in Metals." *Physical Review* 54 (1938): 899.
- Podolak, K. R., M. G. Birke, N. Janke-Gilman, and R. F. Willis. "Distinguishing magnetic behavior on the Slater-Pauling curve applied to nanoscale thin films." 2006.
- Slater, J. C. "The Ferromagnetism of Nickel. II. Temperature Effects." *Physical Review* 49 (1936): 931.
- Thole, B. T., P. Carra, F. Sette, and G. van der Laan. "X-ray Circular Dichroism as a Probe of Orbital Magnetization." *Physical Review Letters* 68 (1992): 1943-1946.
- Walock, M. J., H. Ambaye, M. Chshiev, F. R. Klose, W. H. Butler, and G. J. Mankey. "High magnetization FeCo/Pd multilayers." *Journal of Vacuum Science and Technology A* 26, no. 4 (2008): 731-734.
- Wu, R., and A. J. Freeman. "Limitation of the magnetic circular dichroism spin sum rule for transition metals and importance of the magnetic dipole term." *Physical Review Letters* 73 (1994): 1994-1997.

Yildiz, F., et al. "Strongly enhanced orbital moment by reduced lattice symmetry and varying composition of  $\text{Fe}_{1-x}\text{Co}_x$  alloy films." *Physical Review Letters* 100 (2008): 037205.

Zabel, H. "Neutron reflectivity of spintronic materials." *Materials Today*, 2006: 42.